energies

MDPI

Article

Research on Anti-Icing Performance of Graphene Photothermal Superhydrophobic Surface for Wind Turbine Blades

Yujun Gou [1], Jia Han [1], Yida Li [1], Yi Qin [1], Qingan Li [2,3,*] and Xiaohui Zhong [2,3,4,*]

[1] College of Metallurgy and Energy, North China University of Technology, Tangshan 063210, China
[2] Institute of Engineering Thermophysics, Chinese Academy of Sciences, Beijing 100190, China
[3] Key Laboratory of Wind Energy Utilization, Chinese Academy of Sciences, Beijing 100190, China
[4] Dalian National Laboratory for Clean Energy, Dalian 116023, China
* Correspondence: liqingan@iet.cn (Q.L.); zhongxiaohui@iet.cn (X.Z.)

Abstract: In this study, graphene is used as a photothermal material, which is added to the SiO_2 superhydrophobic solution treated with fluorine silane, and then sprayed on the copper plate surface to prepare a new type of photothermal superhydrophobic surface with contact angles up to 160.5° and 159.8°. Under the conditions of natural convection, the effects of photothermal superhydrophobic surfaces on droplet condensation, freezing, and frost growth are investigated in different environments. The results show that the photothermal superhydrophobic surface can not only delay the freezing of surface droplets, prolong the freezing time of droplets, and reduce the thickness of the frost layer, but also allow for the rapid removal of droplets under near-infrared (NIR) irradiation. If the droplet is irradiated by an infrared laser emitter while the cooling system is still turned on, the internal temperature of the droplet will always be higher than the crystallization temperature under the illumination intensity of 2 W/cm^2, and the droplets will not freeze. With the extension of irradiation time, the droplet will evaporate, and the volume of the droplet will decrease. On the basis of summarizing and evaluating the study on the anti-icing performance of superhydrophobic surfaces and the properties of photothermal materials, a new research direction regarding the anti-icing of fan blade surfaces was established. This kind of surface combines the photothermal capabilities of light absorption materials with the micro- and nanostructure of the superhydrophobic surface to improve the anti-icing capability of wind turbine blade surfaces in difficult conditions.

Keywords: superhydrophobic surfaces; de-icing/anti-icing; graphene; photothermal effect

check for updates

Citation: Gou, Y.; Han, J.; Li, Y.; Qin, Y.; Li, Q.; Zhong, X. Research on Anti-Icing Performance of Graphene Photothermal Superhydrophobic Surface for Wind Turbine Blades. *Energies* **2023**, *16*, 408. https://doi.org/10.3390/en16010408

Academic Editor: Theocharis Tsoutsos

Received: 14 November 2022
Revised: 16 December 2022
Accepted: 24 December 2022
Published: 29 December 2022

Copyright: © 2022 by the authors. Licensee MDPI, Basel, Switzerland. This article is an open access article distributed under the terms and conditions of the Creative Commons Attribution (CC BY) license (https://creativecommons.org/licenses/by/4.0/).

1. Introduction

With the popularization and application of clean new energy advocated by the state, wind energy has become one of the important directions of new energy development. However, the icing phenomenon of wind turbine blades restricts the application of wind energy. Effectively solving the icing problem of wind turbine blades is one of the key technical problems to improve the conversion and utilization rate of wind energy. At present, the research on the anti-icing of wind turbine blades mainly involves two major types [1], active de-icing and passive anti-icing. The active method will increase energy consumption and ancillary equipment, which will limit its popularization and application, while the passive method of anti-icing of superhydrophobic materials inspired by the "lotus leaf effect" [2] has received widespread attention. Superhydrophobic surfaces have the characteristics of high contact angle and low rolling angle due to their micro-nano structure and low surface energy, which can effectively reduce the condensation quantity of water droplets on the surface and the adhesion between the ice layer and the blade surface, thus making the surface have the ability of anti-icing [3,4]. Zhang [5] developed a silicon-based hydrophobic coating on a wind turbine blade by a spraying method. Under the condition of simulating cold rain flow, there was no ice formation on the surface. The contact angle

of the surface remained in a high value after several frost-melting experiments and wear resistance tests.

However, based on the research about the anti-icing performance of superhydrophobic surfaces, it was found that when this surface is applied in low temperatures and high humidity, the anti-icing performance generally deteriorates, and even disappears [6]. Hence, it is very important to improve the anti-icing performance of superhydrophobic surfaces under severe conditions.

Inspired by the photothermal coating of solar collectors, introducing nano photothermal materials to the superhydrophobic coating is a new idea that uses the selective absorption and conversion characteristics of photothermal materials to enhance the ice resistance of the surface under severe conditions.

Photothermal materials with broadband absorption of sunlight could efficiently convert light energy into heat energy. This materials have been widely used in seawater desalination [7], oncotherapy [8], sterilization [9], anti-icing [10,11], and other fields. Taking advantage of the special photothermal conversion performance and the superhydrophobic characteristic, the surface temperature can be maintained above the freezing point in cold conditions, so the droplet freezing will be delayed. Even if the droplets are frozen, the crystals are easy to fall off from the surface for the low adhesion characteristics of the superhydrophobic surface [10,12]. Zhang [13] prepared a photothermal superhydrophobic surface with nano silica and carbon nanotubes, which had excellent photothermal conversion performance. Under laser irradiation, the ice layer can be melted in a short time, which significantly improves the anti-icing efficiency.

Because the hydrophobic groups on the surface of nano-SiO_2 particles were increased and the surface energy was reduced after hydrophobic treatment, and considering that the graphene nanoparticles had photothermal conversion performance, the addition of a certain amount of graphene nanoparticles could not only increase the layered micro-nano structure on the surface, but also delay the freezing of surface droplets under NIR light irradiation. In this study, a simple spraying method was used to combine hydrophobically treated SiO_2 nanoparticles with graphene photothermal nanoparticles to create a superhydrophobic surface with excellent photothermal conversion efficiency. The impacts of the graphene nanoparticles' addition ratios on surface morphology, wettability, anti-icing performance, and photothermal conversion properties were investigated, respectively. The results showed that adding graphene up to a certain proportion did not further increase the surface hydrophobicity, but it did boost photothermal conversion efficiency. This surface with the appropriate addition proportion of graphene not only had good anti-icing performance under various conditions, but also had the good photothermal conversion characteristics that can melt the ice crystals formed on the surface under the irradiation of near-infrared light. These characteristics makes the application of the surface more extensive under adverse conditions.

2. Experiment

2.1. Materials

The physical layer with less graphene (layer number 1~5, sheet diameter 10~50 um) was provided by Suzhou Tanfeng Graphene Technology Co., Ltd. (Suzhou, China). Hydrophobic SiO_2 nanoparticles (diameter 15 nm, specific surface area 300 ± 50 m^2/g) and Epoxy resin with corresponding curing agent and accelerator (E-51) were provided by Shanghai Macklin Biochemical Co., Ltd. (Shanghai, China). 1H,1H,2H,2H-perfluorodecyl triethoxysilane (PFDTES, $C_{16}H_{19}F_{17}O_3Si$) was purchased from Ark (Fogang) Chemical Materials Co., Ltd. (Fogang, China). Acetone and anhydrous ethanol were purchased from Tianjin Damao Chemical Reagent Factory. All reagents were used as is without further purification.

2.2. Preparation of Photothermal Superhydrophobic Surfaces on Copper Substrates

Firstly, we used 800#, 1500#, and 2000# sandpaper to polish the surface of purple copper plates, put them into anhydrous ethanol and acetone solution for ultrasonic cleaning for 15 min to remove the oil stain on the surface, and dried them in an oven for later use. Then, 2 g epoxy resin, the corresponding curing agent, and accelerant dissolved in 50 mL anhydrous ethanol were magnetically stirred for 20 min at room temperature to obtain an epoxy resin solution; we sprayed the solution onto the surface of the treated purple copper plate with a spray gun and placed in an oven at 80 °C for 10 min to pre-cure.

The modified hydrophobic silica suspension was produced by ultrasonic dispersion of 50 mg hydrophobic nano-SiO_2, 30 μL PFDTES, and 30 mL ethanol for 30 min. The next steps included adding graphene into the suspension, ultrasonically dispersing it for 45 min to obtain a hydrophobic dispersion with graphene, spraying the dispersion on the surface of the pre-cured epoxy resin substrate with a spray gun, and curing in an oven for 3 h to obtain the photothermal superhydrophobic surface of graphene. The distance between the spray gun and the substrate during spraying was 40 cm, and the outlet pressure was 0.4 MPa.

2.3. Characterization

The surface morphology was characterized by a scanning electron microscope (SEM, SU8020, Hitachi, Japan). The water contact angle (WCA) was measured at room temperature by the OCA50 Micro contact angle meter (Dataphysics Co., Ltd., Germany), and the average value was taken at five positions. The freezing and melting processes of the droplets were recorded with a CCD camera.

2.4. Experimental Apparatus

Figure 1 depicts a schematic diagram of the experimental setup that mainly consists of four sub-systems: the environmental control system (ultrasonic humidifier, temperature and humidity sensor, and experimental cover), refrigeration system (refrigerated hydrazine and high-precision semiconductor constant temperature table), visualization system (industrial electron microscope, CCD camera, semiconductor cold table, display, and cold light source), and data acquisition system (T-type ultra-fine thermocouple, data acquisition instrument, and computer).

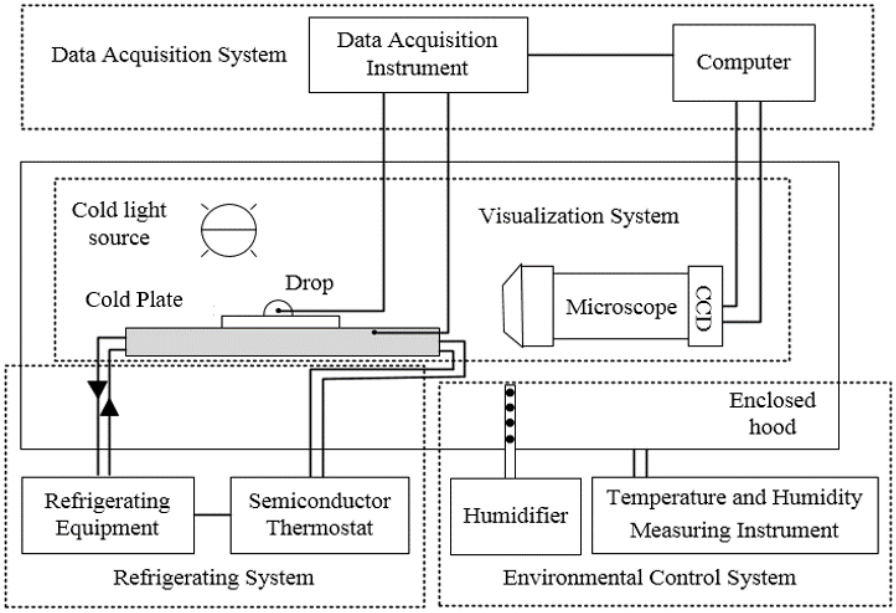

Figure 1. Schematic diagram of the experiment apparatus.

An environmental control system is used to control the working conditions required by the experiment. The humidifier (DRS-03A) is made by Dolac, the humidification range is from 5% to 99%, the accuracy is within 3%, and the maximum humidification rate is up to 3 kg/h. The temperature and humidity measuring instruments are made by Shandong Renke Measurement and Control Technology Company, and the temperature measuring range is −40 °C~80 °C with the accuracy ±0.2 °C, and the humidity range is 0~100%, with the accuracy ±2% RH. The data are measured every 5 s. The whole experiment is carried out in a nearly closed experimental hood, which is made of a transparent acrylic sheet. The refrigeration hydrazine (SLTD1-150S) and the high-precision semiconductor thermostat (SLTD1-150S) are made by Tianjin Jingyi Industry and Trade Co., LTD. Refrigerating hydrazine (accuracy of ±0.01 °C) adopts a chilled water circulation system to reduce the surface temperature and the lowest cooling temperature can reach −25 °C and the temperature control accuracy is ±0.01 °C. The visualization system includes an industrial electron microscope, a CCD camera, a semiconductor cooling stage, a display, and a cold light source. The maximum magnification of the microscope is 60 times. The CCD camera is connected to the microscope, and the image of the microscope is presented through the display. At the same time, the CCD camera has the function of taking pictures and videos, and the image acquisition speed is 30 f/s. The water droplets on the cold surface are titrated by a micro-adjustable single-channel pipette. A T-type thermocouple (±0.1 °C accuracy) is additionally used to measure the internal temperature of the water droplet. The data acquisition system (MT500P-8) is made by Shenhua Electronic Technology Company. It is capable of recording the cold surface temperature during the whole experiment process and the internal temperature change during the freezing process of water droplets. The temperature data are captured every 1 s.

2.5. Anti-Icing Experiments

Before each experiment method, the cold plate surface was first cleaned with absolute ethanol in sequence and then dried naturally. Next, the computer and the cold light source were turned on, and the height of the CCD camera and the focal length of the microscope were adjusted so that we could clearly display the captured image in the computer interface. Before turning on the refrigeration system, we covered the refrigeration table and the coat surface with a plastic film to avoid water vapor adhering to the surface of the specimen during the cooling process. The refrigeration system and the environmental control system were turned on, and the working environment required for the experiment was set. When the surface temperature of the cold plate reached the pre-set value, the counting function of the data acquisition instrument and the recording function of the CCD camera was turned on at the same time to ensure that the data acquisition of images and temperature was carried out simultaneously. Then, we peeled off the plastic film quickly. After the experiment was completed and the data were saved, all equipment was turned off, and the lab bench was organized and cleaned. During the photothermal experiment of frozen droplets, the droplets were irradiated with 808 nm NIR light, and the temperature change inside the droplets was measured with a thermocouple. To ensure the accuracy of the experiments, each set of experiments was repeated three times, and the best results were taken as part of the paper.

3. Results and Discussion

3.1. Surface Wettability

The surface of only the sprayed modified hydrophobic silica suspension was recorded as specimen 1, and the photothermal superhydrophobic surfaces of 25 mg, 40 mg, 55 mg, 70 mg, and 100 mg of graphene added to the modified hydrophobic silica suspension were respectively recorded as specimen 2 to 6. The additional ratio of different contents of graphene and hydrophobic nano-SiO_2 particles affected the surface contact angle. The contact angle of surface water droplets is shown in Figure 2.

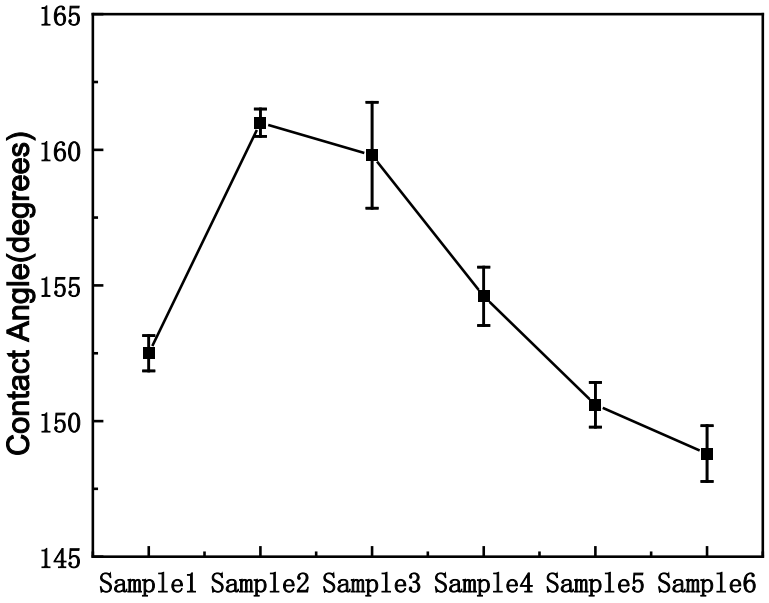

Figure 2. Contact angles of different superhydrophobic surfaces.

The -C_2H_5O group on the surface of PFDTES had a dehydration condensation reaction with the -OH group on the surface of nano-SiO_2, and the silane coupling agent was grafted onto SiO_2 as covalent bonds Si-O-Si. The low surface energy was a key factor in the construction of super-hydrophobicity. PFDTES contained -CF_2 and -CF_3 low surface energy groups, which reduced the surface energy of nano-SiO_2, thus making the prepared suspensions obtain super-hydrophobicity on the surface after spraying. Increasing the roughness of the surface was another factor in building super-hydrophobicity. The addition of a certain amount of graphene made the surface have a greater roughness and increased the contact angle. However, with the increase of graphene nanoparticles, the contact angle of surface water droplets tended to decrease instead. The increase in graphene addition increased the folding and agglomeration between graphene particles, which trapped the droplets in the pore structure, thus increasing the contact area of droplets with the solid surface; the droplets appeared to transition from the Cassie–Baxter state to the Wenzel state, and the surface hydrophobicity decreased, thus the contact angle of water droplets decreased. In this experiment, specimen 2 with a contact angle of 160.5° and specimen 3 with a contact angle of 159.8° were selected for the following experiments for their higher contact angle, which were recorded as Sample A and Sample B, respectively.

The microscopic morphologies of the surfaces of Sample A and Sample B were characterized by SEM, as shown in Figure 3. The hydrophobic nano-SiO_2 and graphene sprayed on the surface gathered on the surface of the specimen to form clusters of different sizes, and the existence of these clusters made the surface have a micro-nano rough structure, and the cluster phenomenon became more obvious with the increase of the graphene addition. According to the Cassie–Baxter wetting model, the presence of cavitation between micro-nano structures reduced the contact area between the droplets and the solid surface, thus improving the surface hydrophobicity.

Therefore, the modification of low surface energy substances effectively reduced the surface energy and improved the hydrophobicity of the surface; the addition of graphene increased the roughness of the surface and further increased the contact angle of the surface. The synergistic effect of both made the surface with excellent superhydrophobic properties.

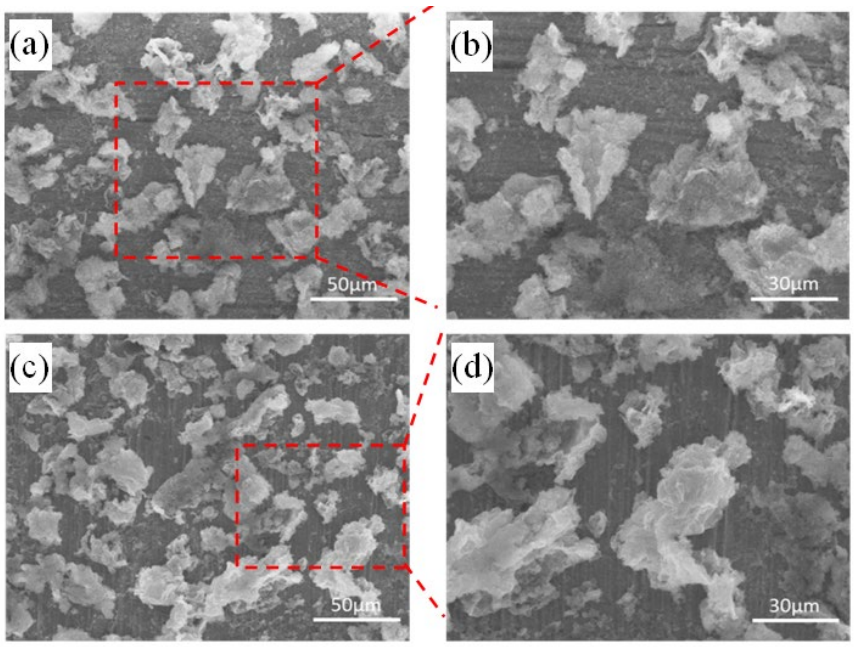

Figure 3. SEM images of samples. (**a**,**b**) Samples A and (**c**,**d**) B are shown. (**a**,**c**) and (**b**,**d**) are different magnification SEM images with a scale of 800×, 1500×, respectively.

3.2. Frost Suppression Performance Test

The experiment was carried out at the ambient temperature of $T_\infty = 30 \pm 0.5$ °C with a relative air humidity of 69 ± 3%. The freezing of condensed droplets and the growth of frost crystals on the surface of the purple copper plate as well as Sample A and Sample B at different moments were recorded by the visualization method.

The cold surface temperature of $T_w = -6$ °C is shown in Figure 4. The droplets on the surface of the purple copper plate grew rapidly. The larger droplets were formed in a short time, irregularly distributed, and closely connected between droplets without gaps. Finally, the condensed droplets in the field of vision were all frozen at 215 s. While the growth rate of condensation droplets on the surface of Sample A and Sample B was significantly slower than that on the surface of the purple copper plate, the super-hydrophobicity of the surface caused droplets to grow in a spherical shape. As condensation proceeds, droplets grew and merged into larger droplets when they came in contact with each other. Due to the low free energy of the surface, a self-jumping phenomenon of droplets would occur: some droplets directly jumped to escape from the surface, and some jumped and fell to the surface again to merge with other droplets and escape from the surface again. The sparse distribution of condensed droplets on the surface was due to the self-jumping phenomenon, and the droplets that remained on the surface existed in a supercooled state for a longer time until the droplets froze. The condensation droplets on the surface of Sample A started to freeze at 1256 s until they were completely frozen within the field of view at 1434 s, and the condensation droplets on the surface of Sample B started to freeze at 965 s and were completely frozen at 1192 s; at this time, a dense layer of frost had grown on the surface of the purple copper plate. The presence of the edge effect caused the condensed droplets to be frozen, starting at the edge and gradually freezing toward the center.

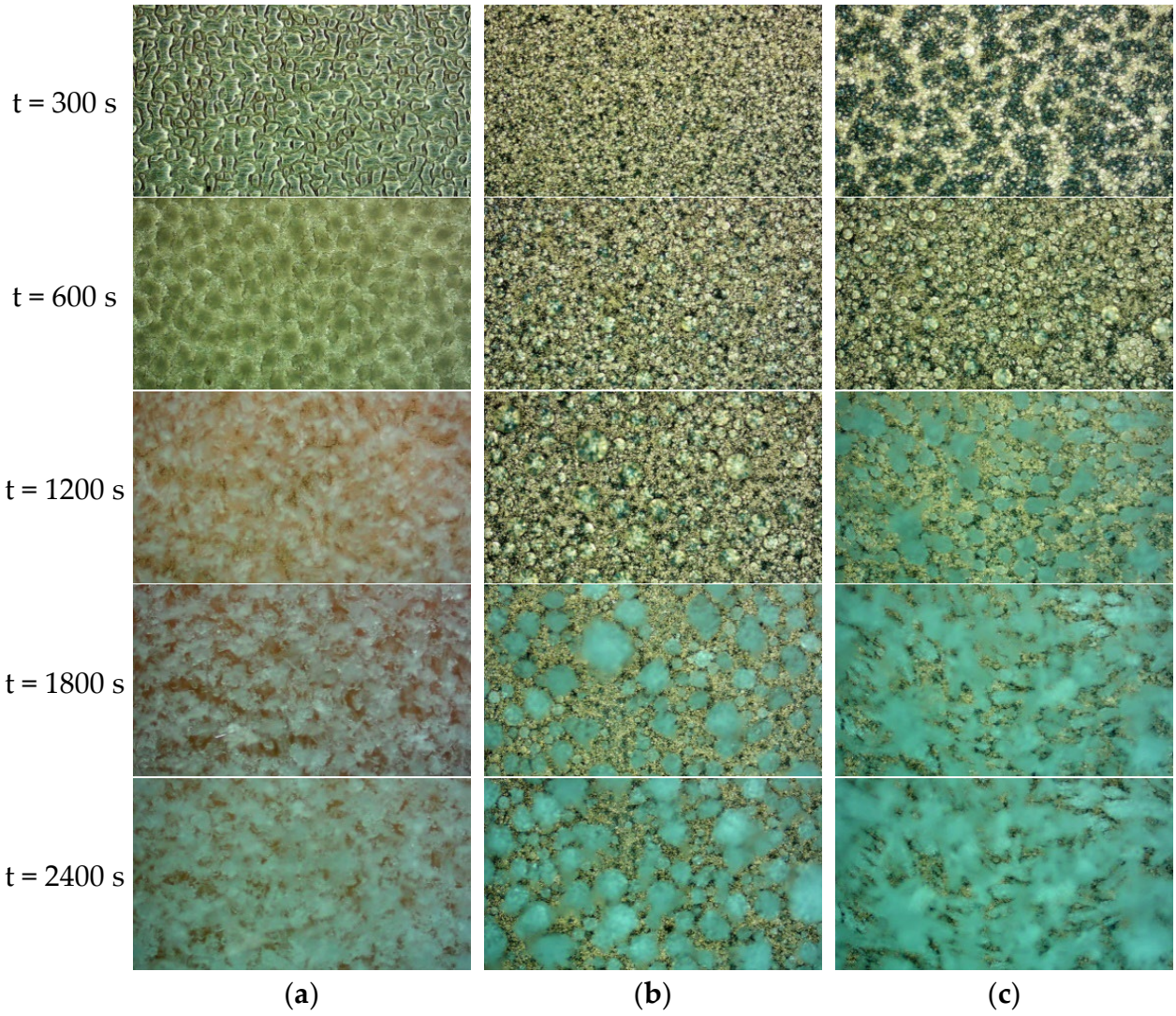

Figure 4. Frost crystal growth process on different surfaces at $T_w = -6$ °C: (**a**) purple copper plate, (**b**) Sample A, and (**c**) Sample B.

To further explore the influence of cold surface temperature on the frost suppression performance of photothermal superhydrophobic surfaces, frosting experiments were conducted at other cold surface temperatures of $T_w = -10$ °C and $T_w = -15$ °C. The experimental phenomenon was similar to that observed when the cold surface temperature was $T_w = -6$ °C. As the cold surface temperature decreased, the condensation droplet size on the surface was smaller, and the rate of droplet freezing was accelerated. At $T_w = -10$ °C, the freezing times of condensation droplets were 134 s, 920 s, and 793 s on the surfaces of the purple copper plate, Sample A, and Sample B, respectively; at $T_w = -15$ °C, the freezing times of condensation droplets were 76 s, 532 s, and 376 s on the surfaces of the purple copper plate, Sample A, and Sample B, respectively. The experiment demonstrated that the photothermal superhydrophobic surfaces could significantly delay the freezing time of condensate droplets compared with the copper plate surface.

Frost thickness was an important index to evaluate the amount of frost on the surface; thus, the frost thickness on the three surfaces was also measured during the experiments at different surface temperatures of −6 °C, −10 °C, and −15 °C. The experiments were all conducted at the ambient temperature of $T_\infty = 31$ °C and an ambient humidity of 70% to ensure the accuracy of the experiments.

Under the three cold surface temperatures, frost always first appeared on the purple copper plate surface. The frost crystals grew vigorously and densely, and the frosting rate

was the fastest. The merging phenomenon occurred between the droplets on both surfaces of Sample A and Sample B. The droplets were spherical in shape, and the contact area with the solid surface was small. The height of the frozen droplets on the superhydrophobic surface was higher than that on the surface of the purple copper plate, and the frost crystals started to grow from the top of the frozen droplets, the cold exchange rate with the cold surface was slow, and the frost layer grew more slowly. Therefore, at the end of the experiment, the frost layers on both photothermal superhydrophobic surfaces were significantly lower than that on the surface of the purple copper plate.

Figure 5 shows the measured frost thickness of the surface of the purple copper plate, the surface of Sample A, and the surface of Sample B at different cold surface temperatures. Figure 5a shows the frost thickness of the three surfaces after the experiment was conducted for 90 min at the cold surface temperature of −6 °C. Figure 5b shows the frost thickness of the three surfaces after the experiment was carried out for 60 min at the cold surface temperature of −10 °C. Figure 5c shows the frost thickness of the three surfaces after 30 min of the experiment when the cold surface temperature was −15 °C.

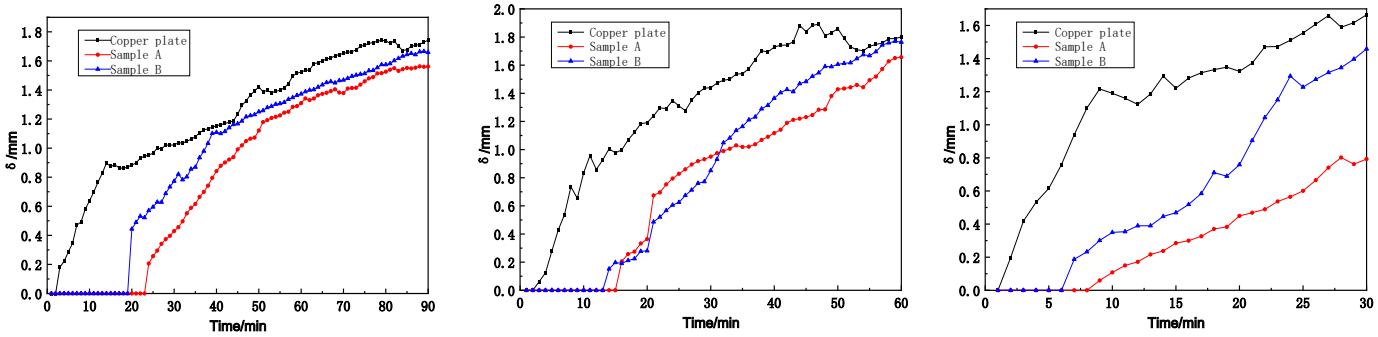

Figure 5. Surface frost thickness of purple copper plate, Sample A, and Sample B. (**a**) T_w = −6 °C, T_∞ = 30 ± 0.5 °C, and Φ = 70 ± 3%; (**b**) T_w = −10 °C, T_∞ = 31 ± 0.5 °C, and Φ = 67 ± 3%; and (**c**) T_w = −15 °C, T_∞ = 30 ± 0.5 °C, and air humidity Φ = 68 ± 3%.

When the cold surface temperature was T_w = −6 °C, the frost layer thickness on the purple copper plate, Sample A, and Sample B respectively reached 1.74 mm, 1.56 nm, and 1.65 nm, after 90 min of the experiment; when the cold surface temperature was T_w = −10 °C, the frost layer thickness on the three surfaces reached 1.82 mm, 1.65 nm, and 1.76 nm, respectively, after 60 min of the experiment; when the cold surface temperature was T_w = −15 °C, the frost thickness of the purple copper plate, Sample A, and Sample B reached 1.66 mm, 0.97 nm, and 1.45 nm, respectively, after 30 min of the experiment.

The results showed that the prepared photothermal superhydrophobic surface A had the lowest frost layer height regardless of that cold surface temperature, which could reduce the number of surface condensation droplets, prolong the freezing time of condensed droplets, reduce the coverage of frost crystals on the surface, and decrease the thickness of the frost layer, exhibiting significant frost suppression performance.

The growth of the frost layer was the phase transition process of vapor from the metastable phase to the stationary phase, i.e., from the vapor phase to the solid phase. In this process, the crystal nucleus was the crystal growth center, and the generation and growth process of the crystal nucleus was called the nucleation process. Ignoring the impact of impurities and wall surfaces, all sites in a homogeneous material system had the same likelihood of forming new phases, which was known as homogeneous nucleation, otherwise called heterogeneous nucleation. Considering the influence of the surrounding environment, the nucleation process in practice was mostly heterogeneous nucleation.

The freezing of droplets on the surface was a heterogeneous nucleation process. The solid–liquid contact surface provided the nucleation position, related to the volume of droplets and the surface contact angle. The larger the surface contact angle, the fewer

nucleation positions. As the contact angle reached 180°, it restrained the growth of icing nucleation. Based on the classical nucleation theory, nucleation occurs only when the nucleation radius is larger than the critical nucleation radius, the droplet freezes, and then the frozen droplet is frosted. The formation of nucleation is the process of new phase generation, where the phase change reduces the Gibbs free energy, and the formation of the solid–liquid interface is needed to overcome a certain free energy barrier, i.e., the Gibbs free energy difference [14] ΔG_c:

$$\Delta G_c = \frac{4}{3}\pi {r_c}^2 \sigma_{LV} f(\theta) = \frac{16\pi {V^1}^2 {\sigma^3}_{LV}}{3\Delta g^2} \quad (1)$$

$$f(\theta) = \frac{\left(2 - 3\cos\theta + \cos^3\theta\right)}{4} \leq 1 \quad (2)$$

where ΔG_c is the critical potential barrier, J; r_c is the critical radius, m; σ_{LV} is the surface tension between air and liquid phases, N/m; V^1 is the volume of a single atom, m3; Δg is the Gibbs free energy difference when a single atom changes from aqueous to crystalline, J; and θ is the contact angle between the water droplet and the solid surface, °.

Under the same external conditions, the value of $f(\theta)$ depended on the contact angle and increased as θ increased, while $f(\theta)$ was a function of ΔG_c. Both of them were positively correlated, so an increase in the contact angle increased the droplet nucleation potential and inhibited droplet freezing, which explained why droplet nucleation was more difficult on photothermal superhydrophobic surfaces.

3.3. Anti-Icing Performance Test

In order to study the internal freezing characteristics of droplets on different cold surfaces and the anti-icing performance of superhydrophobic coatings, three droplets with 20 μL volume were respectively dropped by a pipettor on the surfaces of purple copper plate, Sample A, and Sample B, and the process of droplets freezing was recorded by CCD camera, using the visualization experiment method. The cold surface temperature was set to $T_w = -10$ °C.

The freezing of droplets on cold surfaces occurs through three stages: supercooling, nucleation re-glow, and solidification freezing. As shown in Figure 6, in the supercooling stage shown in Figure 6a,b, the droplets are presented as transparent spheres, and the internal temperature decreased continuously. When the liquid internal temperature reached the crystallization temperature, the latent heat was released to enter the nucleation re-glow stage Figure 6b, which was a very short time. At this time, the droplet lost permeability and was existing in the form of an ice–water mixture; the time of this moment of the droplet was recorded as the droplet start freezing time, and after that, the droplet entered the solidification freezing stage, as shown in Figure 6b–d. With the droplet in the solidification freeze stage, the solid–liquid phase line from the bottom of the droplet began to move up slowly until it was completely frozen, then the top of the droplet grew a papillae structure, and the moment was recorded as the droplet completely frozen time. The middle part of the time from the beginning to the complete freezing was called the continuous freezing time. The droplets on the surface of the purple copper plate started to freeze at 94 s, froze completely at 114 s, and the continuous freezing time was 20 s; the droplets on the surface of Sample A started to freeze at 617 s, froze completely at 658 s, and the continuous freezing time was 41 s; the droplets on the surface of Sample B started to freeze at 501 s, froze completely at 537 s, and the continuous freezing time was 36 s. The results showed that the freezing time and continuous freezing time of the superhydrophobic surface were longer than those of the purple copper plate surface, and the higher the surface contact angle, the longer the extended droplet freezing time.

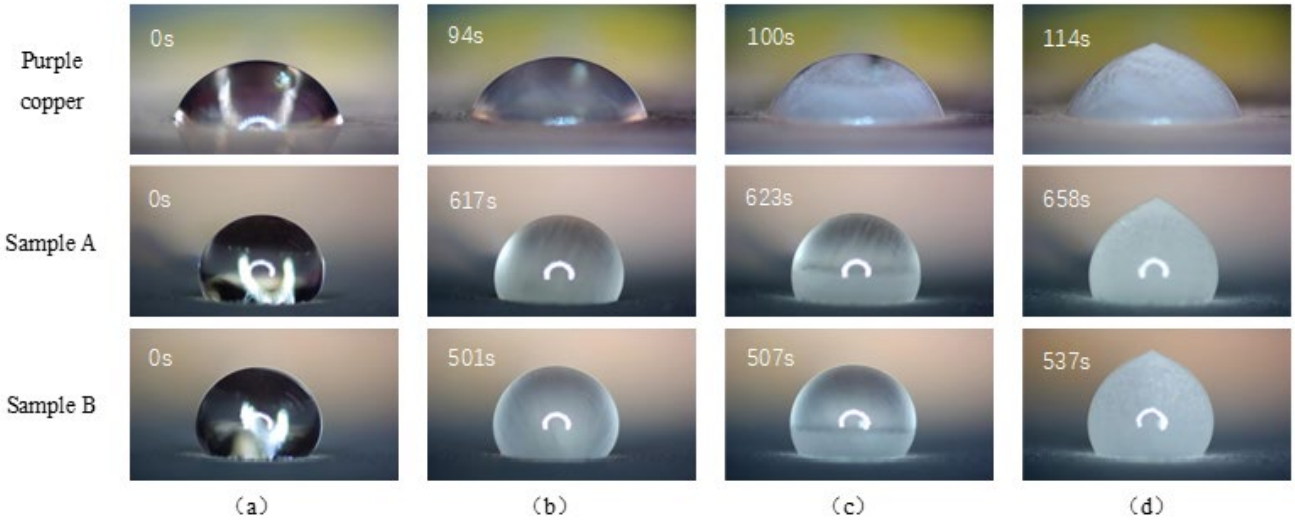

Figure 6. Freezing experiments with droplets on different surfaces, $T_w = -10$ °C. (**a**,**b**) is supercooling stage, (**b**) is nucleation re-glow stage, (**b**–**d**) is solidification freezing stage.

3.4. Photothermal Performance Test

The previous two sections verified that the prepared photothermal superhydrophobic surface had excellent anti-icing performance, which not only delayed the droplet freezing time, but also reduced the surface frost thickness and frost coverage. Due to the excellent photothermal conversion properties of graphene, the prepared surface had an active de-icing performance under certain infrared light. Then, the photothermal conversion performance of this surfaces was studied.

The 808 nm NIR light was selected to irradiate the surface of the purple copper plate, Sample A, and Sample B. The three surfaces were exposed to three different light intensities of 2 W/cm^2, 2.5 W/cm^2, and 3 W/cm^2 for 300 s. The experiments were conducted at room temperature with the ambient temperature of $T_\infty = 18$ °C and the surface temperature of $T_w = 15$ °C. With the data acquisition instrument to record the surface temperature changes, the results are shown in Figure 7. At the moment that the light source was turned on, regardless of the light intensity of the three surfaces in the NIR light, the temperature of the surface of the purple copper plate rose slowly, while the photothermal superhydrophobic surface increased rapidly, which showed extremely strong photo-responsiveness characteristics, and after the temperature rose to a certain value, it tended to stabilize. After the light source was turned off, the surface temperature dropped rapidly to room temperature. Under the illumination intensity of 2 W/cm^2, the temperatures on the surfaces of the purple copper plate, Sample A, and Sample B were increased to 27 °C, 38.9 °C, and 50.3 °C, respectively; under the illumination intensity of 2.5 W/cm^2, the temperatures on the surfaces of the purple copper plate, Sample A, and Sample B were increased to 28.7 °C, 44.5 °C, and 56.9 °C, respectively; under the illumination intensity of 3 W/cm^2, the temperatures on the surfaces of the purple copper plate, Sample A, and Sample B were increased to 33.8 °C, 51.4 °C, and 68.6 °C, respectively. The results showed that the addition of graphene could increase the temperature rise of the surface under NIR light and that the amount of addition was related to the temperature rise of the surface; the more the additive amount, the higher the temperature rose.

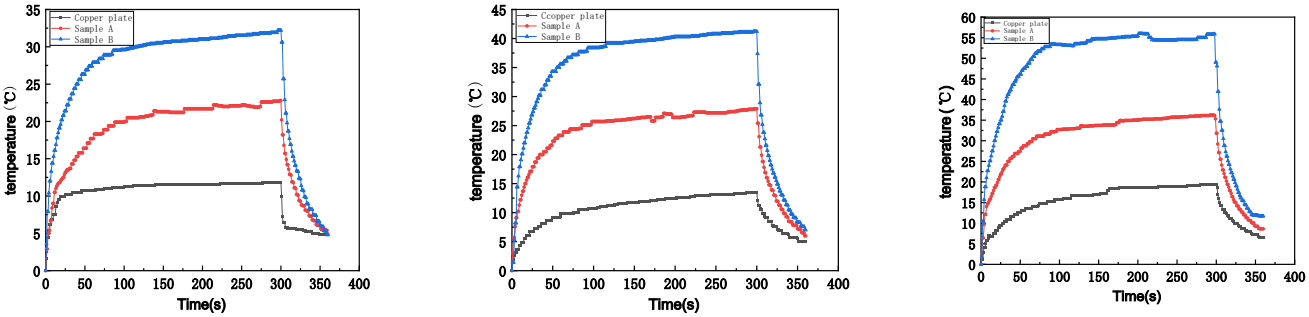

(**a**) 2 W/cm^2 (**b**) 2.5 W/cm^2 (**c**) 3 W/cm^2

Figure 7. The temperature change on the surface of the purple copper plate, Sample A, and Sample B under different illumination intensities.

Graphene had strong light absorption in the visible-near infrared region. The constructed superhydrophobic surface could effectively trap light due to the micro-nanostructure, and the light was trapped in the layered structure and reflected several times until it was fully absorbed internally to achieve photothermal conversion. Graphene was formed by the sp2 hybridization of carbon atoms. Each C atom had four valence electrons, three of which were shared with neighboring C atoms to form σ-electrons, and the other valence electron formed a delocalized π-electron. The valence band was the region with the highest energy in the orbitals where the electrons were located, and the conduction band was the lowest energy part of the empty orbitals, with the valence band having higher energy than the conduction band. The electrons in the valence band were called σ-electrons and π-electrons, and the orbitals in the conduction band were called σ*-orbitals and π*-orbitals. The polyatomic layer structure of graphene with few layers gave it a central asymmetry. When there was external energy input, electronic transitions such as σ-σ *, σ-π *, π-σ *, and π-π * will occur. The electrons transferred energy to the surface through electron–phonon coupling during the leap, which raised the surface temperature [15]. The electromagnetic wavelength at the π-π* electron transition was 51–1771 nm. When the photothermal surface was irradiated with 808 nm NIR light, graphene absorbed the wavelength in this band and transferred the photon energy to π electrons for an interband transition, which caused lattice vibration during the transition and generated energy to raise the surface temperature.

In terms of internal plasma resonance, when NIR light irradiated the surface of graphene particles, the incident photon frequency matched the vibration frequency of graphene electrons, which made graphene have strong absorption of the energy generated by NIR light and excite the electrons outside the carbon atom on one side to move to the carbon atom on the other side, which made the electrons on that side pile up and generate an electric field due to polarization, causing electron vibration. The vibration phenomenon generated by electrons inside graphene could raise the temperature of the surface.

3.5. Photothermal De-Icing Performance

The results in Section 3.3 show that the prepared photothermal superhydrophobic surfaces had excellent anti-icing properties. Considering the photothermal conversion characteristics of these surfaces, the de-icing properties of these surfaces under NIR light were further investigated. The experiments were conducted at a cold surface temperature of $T_w = -10$ °C. Three droplets with 20 μL volume were respectively dropped by a pipettor on the surfaces of purple copper plate, Sample A, and Sample B. About 20 min later, since at the test beginning, the droplets were completely frozen, the NIR laser emitter was turned on. The light source was emitted at a distance of 30 cm from the cold surface with an incidence angle of 45°. The frozen droplets were irradiated with illumination intensities of 2 W/cm^2, 2.5 W/cm^2, and 3 W/cm^2, respectively, and the whole process of droplet melting was recorded with a CCD camera.

Figure 8 shows the frozen droplet on the purple copper plate surface at different test times under the illumination intensity of 3 W/cm^2. There were not any photothermal particles on the surface of the purple copper plate, so it does not have the ability of photothermal conversion, and the droplets have almost no change in morphology for 600 s.

Figure 8. Droplet morphology on the surface of the purple copper plate under the illumination intensity of 3 W/cm^2.

Considering the frozen droplets on the surface of Sample A and Sample B under the irradiation of the NIR light source, the droplet morphology changed significantly, as shown in Figures 9–11. The photothermal effect of graphene increased the temperature of the surface rapidly, and the droplet melting process first started at the boundary of the droplet walls. With continuous heat transfer upward, the papillae structure at the top of the frozen droplet disappeared, and the droplet changed from a solid to an ice–water mixture; gradually, the nucleus inside the droplet disappeared, and the frozen droplet was reverted to a transparent liquid droplet. The whole melting process took a very short time that no more than 160 s while the cooling system operated continuously. Under the illumination intensities of 2 W/cm^2, 2.5 W/cm^2, and 3 W/cm^2, the complete melting times of frozen droplets on the surface of Sample A were 160 s, 60 s, and 30 s, respectively, and on the surface of Sample B were 120 s, 40 s, and 20 s, respectively.

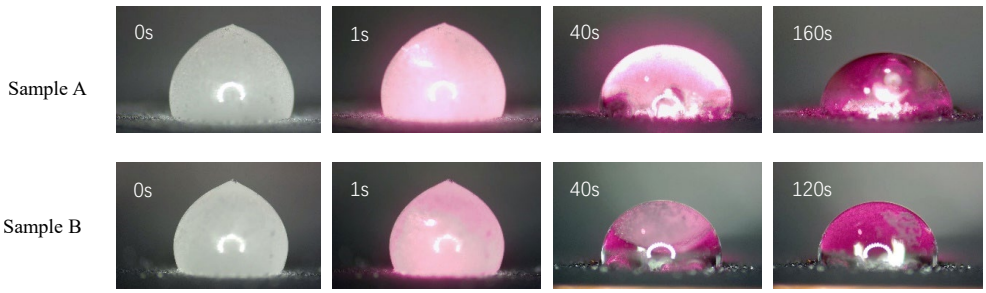

Figure 9. The melting morphology of frozen droplets on the surface of Sample A and Sample B under 2 W/cm^2 illumination intensity.

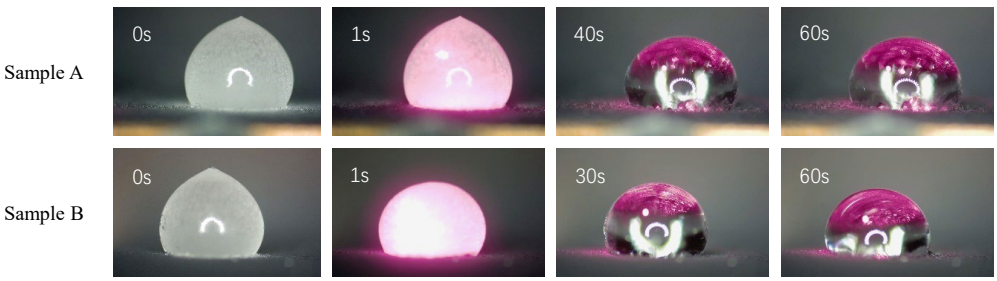

Figure 10. The melting morphology of frozen droplets on the surface of Sample A and Sample B under 2.5 W/cm^2 illumination intensity.

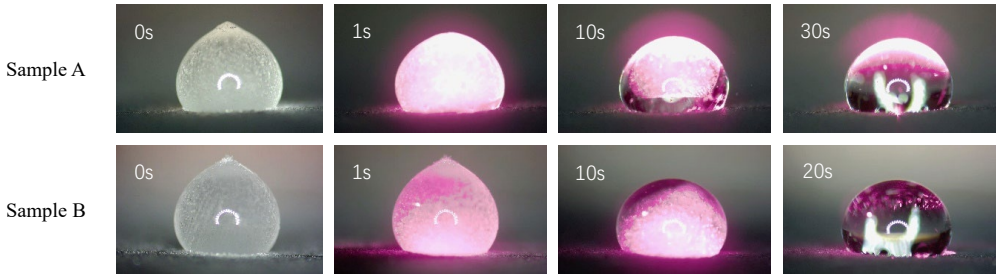

Figure 11. Melting morphology of frozen droplets on the surface of Sample A and Sample B under 3 W/cm^2 illumination intensity.

If the test time was extended for 1 h, the droplets on the surface of the two samples did not freeze for all the time while the refrigeration system always operated. The internal temperature of the droplets was measured by thermocouples, and it was found that the internal temperature was always above 0 °C, which was higher than the crystallization temperature of the droplets, as shown in Figure 12. Since the amount of graphene added to the two kinds of samples was different, the surface with more graphene added had higher heat transfer ability, which resulted in a higher internal temperature of the droplet. At the same time, the sizes of the droplets both decreased continuously under the irradiation of infrared light on the two sample surfaces as shown in Figure 13. While on the Sample B surface, the droplet volume decreased more because it contained more graphene particles. The droplet volume decrease may be caused by the evaporation at the boundary of droplet caused by the heat converted from infrared light through graphene.

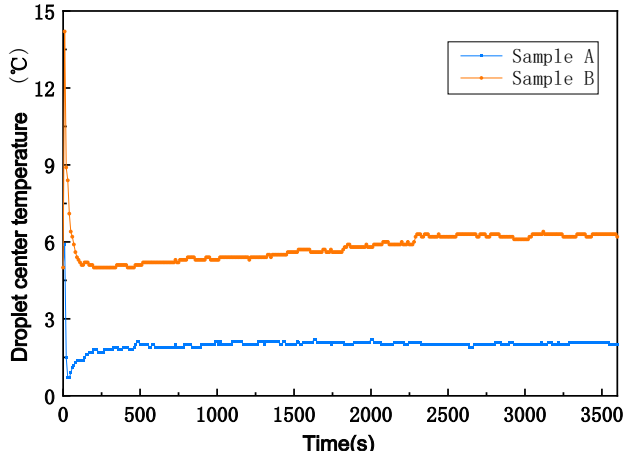

Figure 12. Inside temperature change of droplets under 2 W/cm^2 illumination intensity.

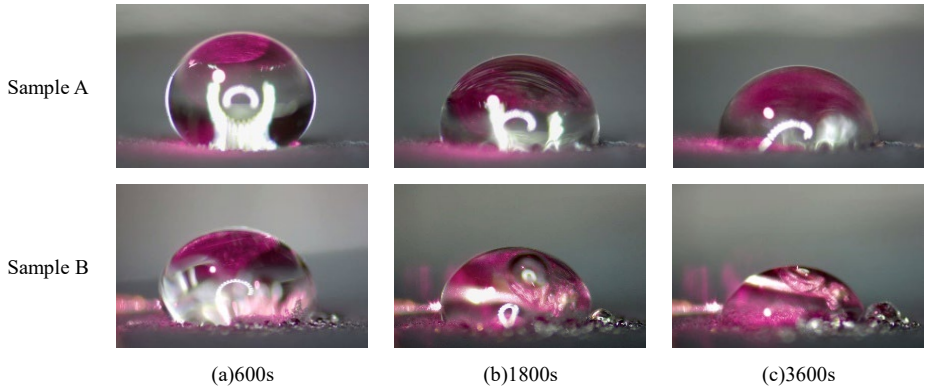

Figure 13. Changes in droplet morphology on the surface of Sample A and Sample B under 2 W/cm^2 illumination intensity.

The above results show that the prepared photothermal superhydrophobic surface had excellent photothermal conversion performance under different illumination intensities since the graphene particles in the surfaces can transfer the light energy into heat that causes the surface temperature to rise and the frozen droplets to melt. The stronger the illumination intensity was, the more heat was transferred, and the droplets melted faster. The more graphene added, the better photo thermal conversion effect, the faster the frozen droplets melted, and the more the droplet volume decreased; finally, the droplet even disappeared.

4. Conclusions

A photothermal superhydrophobic surface with a high contact angle was created on a purple copper plate using a two-step spraying process. By conducting passive anti-icing and active de-icing experiments on the surface, the following conclusions were obtained.

(a) Fluorine silane was used to enhance the hydrophobic groups on the surface of SiO_2 nanoparticles, improving their hydrophobicity. Through the inclusion of graphene nanoparticles, the hydrophobicity of the surface was further boosted.
(b) The prepared surface had excellent anti-icing performance by delaying surface condensation droplets and prolonging droplet freezing time. It also exhibited a spontaneous self-jumping phenomenon when condensation droplets condensed on the surface, which lowered the number of surface condensation droplets and the amount of surface frost crystal.
(c) The surface displayed great light response sensitivity and quickly rose in temperature when exposed to NIR light. The de-icing efficiency under NIR irradiation was significantly improved, and the active de-icing performance was also excellent when the frozen droplets were exposed to NIR light. Even after an hour, the droplets on the cold surface did not freeze, and the droplets' volume decreased. The photothermal superhydrophobic surfaces possessed very excellent anti-icing and de-icing performance under various severe conditions.

The developed photothermal superhydrophobic surface was solely examined for its ability to prevent icing and suppress frost in an experimental setting; actual use was not considered. The next stage will be to spray the prepared suspension onto the wind turbine blade and assess the anti-icing efficacy of the blade surface under actual conditions.

Author Contributions: Conceptualization, X.Z. and Q.L.; writing—original draft preparation, J.H. and Y.L.; writing—review and editing, Y.G. and Y.Q.; supervision, X.Z. All authors have read and agreed to the published version of the manuscript.

Funding: This research received no external funding.

Conflicts of Interest: The authors declare no conflict of interest.

References

1. Mo, Q.; Wang, G.; Guo, R.; Li, L.; Liu, Y. Wind turbine blade icing condition and anti-icing deicing measuresx. *Sci. Technol. Eng.* **2022**, *22*, 9017–9024.
2. Onda, T.; Shibuichi, S.; Satoh, N.; Tsujii, K. Super-Water-Repellent Fractal Surfaces. *Langmuir* **1996**, *12*, 2125–2127. [CrossRef]
3. Hu, J.; Jiang, G. Superhydrophobic coatings on iodine doped substrate with photothermal deicing and passive anti-icing properties. *Surf. Coat. Technol.* **2020**, *402*, 126342. [CrossRef]
4. Sarshar, M.A.; Song, D.; Swarctz, C.; Lee, J.; Choi, C.H. Anti-Icing or Deicing: Icephobicities of Superhydrophobic Surfaces with Hierarchical Structures. *Langmuir* **2018**, *34*, 13821–13827. [CrossRef] [PubMed]
5. Zhang, L.B.; Zhang, H.X.; Liu, Z.J.; Jiang, X.Y.; Agathopoulos, S.; Deng, Z.; Gao, H.Y.; Zhang, L.; Lu, H.P.; Deng, L.J.; et al. Nano-silica anti-icing coatings for protecting wind-power turbine fan blades. *J. Colloid Interface Sci.* **2022**, *630*, 1–10. [CrossRef] [PubMed]
6. Li, W.; Zhan, Y.; Yu, S. Applications of superhydrophobic coatings in anti-icing: Theory, mechanisms, impact factors, challenges and perspectives. *Prog. Org. Coat.* **2021**, *152*, 106117. [CrossRef]
7. Shokrollahi, M.; Asadollahi, M.; Mousavi, S.A.; Rajabi-ghahnavieh, A.; Behzadi-Sarok, M.; Khayet, M. Photothermally heated and mesh-gridded solar-driven direct contact membrane distillation for high saline water desalination. *Int. J. Heat Mass Transf.* **2022**, *199*, 123442. [CrossRef]

8. Li, H.; Zhao, Y.; Kolesnikov, I.; Xu, S.; Chen, L.; Bai, G. Multifunctional rare earth ions-doped Ba2LaF7 nanocrystals for simultaneous temperature sensing and photothermal therapy. *J. Alloy. Compd.* **2022**, 167535. [CrossRef]
9. Park, E.; Selvaraj, R.; Kim, Y. High-efficiency photothermal sterilization on PDMS film with Au@CuS yolk-shell nanoparticles. *J. Ind. Eng. Chem.* **2022**, *113*, 522–529. [CrossRef]
10. Xie, Z.; Wang, H.; Li, M.; Tian, Y.; Deng, Q.; Chen, R.; Zhu, X.; Liao, Q. Photothermal trap with multi-scale micro-nano hierarchical structure enhances light absorption and promote photothermal anti-icing/deicing. *Chem. Eng. J.* **2022**, *435*, 135025. [CrossRef]
11. Chen, H.; Wu, S.L.; Wang, H.L.; Wu, Q.Y.; Yang, H.C. Photothermal Devices for Sustainable Uses Beyond Desalination. *Adv. Energy Sustain. Res.* **2021**, *2*, 2000056. [CrossRef]
12. Wu, S.; Du, Y.; Alsaid, Y.; Wu, D.; Hua, M.; Yan, Y.; Yao, B.; Ma, Y.; Zhu, X.; He, X. Superhydrophobic photothermal icephobic surfaces based on candle soot. *Proc. Natl. Acad. Sci. USA* **2020**, *117*, 11240–11246. [CrossRef]
13. Zhang, F.; Xu, D.; Zhang, D.; Ma, L.; Wang, J.; Huang, Y.; Chen, M.; Qian, H.; Li, X. A durable and photothermal superhydrophobic coating with entwinned CNTs-SiO_2 hybrids for anti-icing applications. *Chem. Eng. J.* **2021**, *423*, 130238. [CrossRef]
14. Wang, H.; He, G.; Tian, Q. Effects of nano-fluorocarbon coating on icing. *Appl. Surf. Sci.* **2012**, *258*, 7219–7224. [CrossRef]
15. Li, Z.; Lei, H.; Kan, A.; Xie, H.; Yu, W. Photothermal applications based on graphene and its derivatives: A state-of-the-art review. *Energy* **2021**, *216*, 119262. [CrossRef]

Disclaimer/Publisher's Note: The statements, opinions and data contained in all publications are solely those of the individual author(s) and contributor(s) and not of MDPI and/or the editor(s). MDPI and/or the editor(s) disclaim responsibility for any injury to people or property resulting from any ideas, methods, instructions or products referred to in the content.